

Influence of the local scattering environment on the localization precision of single particles

Supplementary information

Dorian Bouchet,¹ Rémi Carminati,² and Allard P. Mosk¹

¹*Nanophotonics, Debye Institute for Nanomaterials Science, Utrecht University, P.O. Box 80000, 3508 TA Utrecht, the Netherlands*

²*Institut Langevin, ESPCI Paris, PSL University, CNRS, 1 rue Jussieu, 75005 Paris, France*

I. ELECTRODYNAMICS SIMULATIONS BASED ON THE COUPLED DIPOLE METHOD

In this section, we describe the numerical approach used to compute the average value of the intensity in the image plane. The model system is a set of N_s infinite cylinders, confined within an area of transverse dimension $L_z = 10\lambda$ and with a larger longitudinal dimension ($L_x = 50\lambda$) in order to minimize finite-size effects. A small exclusion radius is defined around the scatterers to prevent them from overlapping. The system is illuminated by an incident field polarized along the longitudinal axis of the cylinders. The scalar wave equation is then solved using a numerical approach based on the coupled dipole method [1], which is an exact formulation in the limit of small cross-sections for the scatterers. Using this model, the field $E(\mathbf{r}_j)$ at the position of the j -th scatterer is expressed by

$$E(\mathbf{r}_j) = E_0(\mathbf{r}_j) + k^2 \sum_{\substack{n=0 \\ n \neq j}}^{N_s-1} G_0(\mathbf{r}_j, \mathbf{r}_n) \alpha_n E(\mathbf{r}_n), \quad (\text{S1})$$

where \mathbf{r}_n is the position of the n -th scatterer, $E_0(\mathbf{r}_n)$ is the incident field at this position and α_n is the polarizability of the scatterer. For 2D systems, the free-space Green function is

$$G_0(\mathbf{r}, \mathbf{r}') = \frac{i}{4} H_0^{(1)}(k|\mathbf{r} - \mathbf{r}'|), \quad (\text{S2})$$

where $H_0^{(1)}$ is the Hankel function of the first kind of order 0. Equation (S1) defines a set of N_s linear equations that are solved using standard computational routines. The field at any position \mathbf{r} can then be calculated using

$$E(\mathbf{r}) = E_0(\mathbf{r}) + k^2 \sum_{n=0}^{N_s-1} G_0(\mathbf{r}, \mathbf{r}_n) \alpha_n E(\mathbf{r}_n). \quad (\text{S3})$$

Finally, the field in the camera plane is calculated by applying a low-pass filter to the field evaluated at $z = L_z$. Low-pass filtering of the field is performed by convolving it with the product of the cardinal sine function and a Blackman window. In this way, we filter the frequencies higher than $K_{max} = k \text{NA}$ with a transition bandwidth

that we set to be on the order of $K_{max}/10$. The numerical aperture of the detection objective is set to $\text{NA} = 1$ in the simulations. Assuming that the imaging system has a unitary magnification and choosing a small pixel dimension ($\Delta x = \lambda/10$), the average value for the signal measured by the i -th pixel of the camera simply reads $I_i \simeq \Delta x |E_i|^2$ where E_i is the value of the filtered field at the i -th sampling point.

II. MINIMUM VARIANCE UNBIASED ESTIMATOR FOR THE LINEAR MODEL

In this section, we show that we can obtain an explicit expression for an unbiased estimator that reaches the CRLB, in the limit of small parameter variations and for a large number of detected photons. Let us assume that the measured data \mathbf{X} can be described by a linear model such as

$$\mathbf{X} = \mathbf{I} + \mathbf{J}\mathbf{d} + \mathbf{w}, \quad (\text{S4})$$

where we introduced the intensity vector $\mathbf{I} = (I_1(\boldsymbol{\theta}_0), \dots, I_N(\boldsymbol{\theta}_0))^T$, the displacement vector $\mathbf{d} = (\Delta\theta_1, \dots, \Delta\theta_K)^T$, the noise vector \mathbf{w} and the Jacobian matrix \mathbf{J} expressed by

$$\mathbf{J} = \begin{pmatrix} \partial I_1 / \partial \theta_1 & \partial I_1 / \partial \theta_2 & \cdots & \partial I_1 / \partial \theta_K \\ \partial I_2 / \partial \theta_1 & \partial I_2 / \partial \theta_2 & \cdots & \partial I_2 / \partial \theta_K \\ \vdots & \vdots & \ddots & \vdots \\ \partial I_N / \partial \theta_1 & \partial I_N / \partial \theta_2 & \cdots & \partial I_N / \partial \theta_K \end{pmatrix}. \quad (\text{S5})$$

We assume that the intensity vector \mathbf{I} and the Jacobian matrix \mathbf{J} are known. In practice, this can be achieved with a calibration step, which consists of measuring the intensity and its derivative at $\boldsymbol{\theta}_0$. Moreover, we assume that the noise vector \mathbf{w} follows a normal distribution $\mathcal{N}(\mathbf{0}, \mathbf{C})$, where \mathbf{C} is the covariance matrix. The normal distribution is indeed a good approximation of the Poisson distribution for a large number of detected photons. Only diagonal terms of the covariance matrix are non-zero, as events detected by different pixels are statistically independent. Thus, the covariance matrix is

expressed by

$$\mathbf{C} = \begin{pmatrix} I_1(\boldsymbol{\theta}_0) & 0 & \cdots & 0 \\ 0 & I_2(\boldsymbol{\theta}_0) & \cdots & 0 \\ \vdots & \vdots & \ddots & \vdots \\ 0 & 0 & \cdots & I_N(\boldsymbol{\theta}_0) \end{pmatrix}. \quad (\text{S6})$$

Under these assumptions, the minimum variance unbiased estimator for \mathbf{d} reaches the Cramér-Rao bound [2], and is given by

$$\hat{\mathbf{d}} = (\mathbf{J}^T \mathbf{C}^{-1} \mathbf{J})^{-1} \mathbf{J}^T \mathbf{C}^{-1} (\mathbf{X} - \mathbf{I}). \quad (\text{S7})$$

This can be written in the following form:

$$\hat{\mathbf{d}} = \mathcal{F}^{-1}(\boldsymbol{\theta}_0) \sum_{i=1}^N \nabla_{\boldsymbol{\theta}} I_i \left[\frac{X_i - I_i(\boldsymbol{\theta}_0)}{I_i(\boldsymbol{\theta}_0)} \right], \quad (\text{S8})$$

where we introduced the Fisher information matrix $\mathcal{F}(\boldsymbol{\theta}_0)$ and the differential operator $\nabla_{\boldsymbol{\theta}} = (\partial/\partial\theta_1, \dots, \partial/\partial\theta_K)^T$. Finally, note that, since only maximum likelihood estimators can be unbiased and efficient, then the estimator expressed by Eq. (S8) is necessarily the maximum likelihood estimator.

III. INFLUENCE OF ERRORS ON THE CONFIGURATION OF THE MEDIUM

In this section, we study the robustness of estimations regarding random errors on the position of the dipoles constituting the scattering environment. To this end, we generate 1000 random configurations of the scattering environment, for three different optical thicknesses (controlled by changing the number of scatterers in the medium). For all calculations, we consider a wavelength $\lambda = 633$ nm and an average incident intensity $I_0 = 10^4$ photons per μm . For each configuration, we determine the optimized wavefront for the coordinate x_0 , and we construct the estimator defined by Eq. (S8). We then modify the position of all scatterers constituting the scattering environment according to a Gaussian distribution of variance σ_G^2 , compute the transmitted intensity, and add a random Poisson noise to this intensity. We finally use these numerically-generated data to perform estimations of x_0 via the previously-constructed estimator.

We show in Fig. S1 the (arithmetic) average standard error on the estimates σ_{est} as a function of standard deviation of the structural noise σ_G in the single-scattering regime ($L_z/\ell = 0.80$, dark blue points), in the moderate multiple-scattering regime ($L_z/\ell = 2.3$, medium blue points) as well as deeper in the multiple-scattering regime ($L_z/\ell = 6.5$, light blue points). The influence of σ_G on the average standard error on the estimates strongly depends on the scattering strength of the environment. Indeed, for the different cases numerically studied, adding

a structural noise with a standard error of 1 nm leads to an average standard error on the estimates of 8.0 nm (for $L_z/\ell = 0.80$), 15 nm (for $L_z/\ell = 2.3$) or 61 nm (for $L_z/\ell = 6.5$).

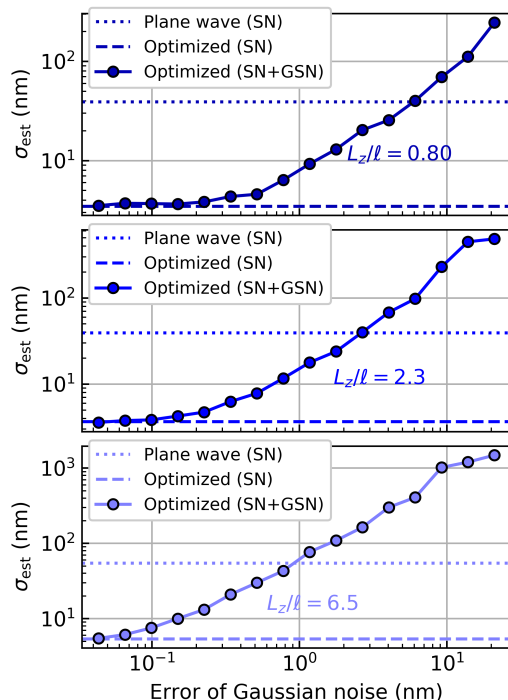


FIG. S1. Average standard error on the estimates as a function of the standard deviation σ_G of the Gaussian noise applied to the dipoles constituting the scattering environment, in the single-scattering regime ($L_z/\ell = 0.80$, top panel), in the moderate multiple-scattering regime ($L_z/\ell = 2.3$, middle panel) and deeper in the multiple-scattering regime ($L_z/\ell = 6.5$, bottom panel). SN: shot noise, GSN: Gaussian structural noise.

We can compare these values to the one obtained in the shot-noise limit without structural noise ($\sigma_G = 0$). In the case of optimized illumination, the average standard error is 3.5 nm (for $L_z/\ell = 0.80$), 3.7 nm (for $L_z/\ell = 2.3$), and 5.4 nm (for $L_z/\ell = 6.5$). In contrast, plane-wave illuminations leads to an average standard error of 39 nm (for $L_z/\ell = 0.80$), 39 nm (for $L_z/\ell = 2.3$) and 55 nm (for $L_z/\ell = 6.5$). Thus, in the single-scattering regime and in the moderate multiple-scattering regime, optimized illumination with a structural noise of 1 nm leads to a smaller error than plane-wave illumination with no structural noise. This demonstrates that, with a prior knowledge of the order of 1 nm as available with current lithography techniques [3], studying and optimizing the estimation precision in the shot-noise limit can be directly relevant to the control of manufactured samples, in the single-scattering regime and in the moderate multiple-scattering regime. Only when stronger multiple scattering occurs (for $L_z/\ell = 6.5$), it appears that

adding a structural noise of 1 nm degrades the standard error on the estimates as much as using a plane wave instead of an optimized wavefront. Nevertheless, it must be noted that the estimation precision could be further improved by building an estimator that takes into account the incompleteness of the prior knowledge available on the scattering environment, instead of using an estimator based on incorrect prior knowledge.

IV. LOG-NORMAL DISTRIBUTION OF THE CRAMÉR-RAO LOWER BOUND

In this section, we show that the CRLB follows a log-normal distribution in the multiple-scattering regime. Indeed, the probability density function followed by the CRLB is correctly fitted by a log-normal distribution for a wide range of scattering mean free path in the multiple scattering regime (Fig. S2), thereby justifying to calculate the geometric moments of the distributions rather than the arithmetic ones. As mentioned in the manuscript, decreasing kl leads to a broadening of the density function, as well as an increase of the average CRLB.

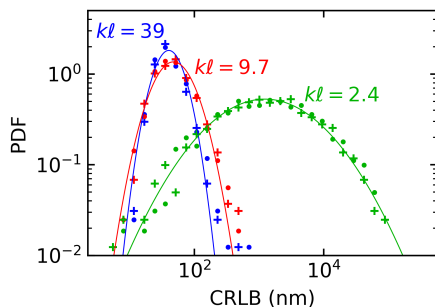


FIG. S2. Probability density functions followed by the CRLB on the coordinate x_0 (data points) and z_0 (crosses) for different values of the normalized mean free path. Solid lines are log-normal fits to the data.

V. CONVERGENCE OF THE OPTIMIZATION ALGORITHM

In this section, we show that the values of the optimized CRLB weakly depend on the initial guess fed to the optimization algorithm, and that the optimized field distributions are strongly correlated. The algorithm that we implemented is based on simulated annealing, which is an adaptation of the Metropolis-Hastings algorithm for approximating the global optimum of a cost function [4]. The initial guess for the phases of the N_e elements of the

SLM is randomly chosen, and the CRLB is iteratively optimized using approximately $700 \times N_e$ function evaluations. Furthermore, at the end of each optimization, we systematically perform a final optimization step using a quasi-Newton method.

In order to test the performance of the algorithm, we use the configuration displayed in the manuscript, in the diffusive regime ($kl = 9.7$). We successively minimize C_x and C_z using 64 SLM elements, and we repeat this optimization procedure for 100 randomly generated initial guesses of the input phases. We can assess the dispersion of the resulting distributions (Fig. S3, upper panels) using the 1-sigma interval defined as $[\mu_g/\sigma_g; \mu_g\sigma_g]$ where μ_g and σ_g are respectively the geometric mean and standard deviation of the distribution. The 1-sigma intervals are [5.638 nm; 5.646 nm] for the optimization of C_x and [3.646 nm; 3.651 nm] for the optimization of C_z . The dispersion of these distributions is small as compared to the dispersion of the distribution observed when optimizing the CRLB for each coordinate over 1000 different random configurations, with a 1-sigma interval equal to [3.412 nm; 8.425 nm].

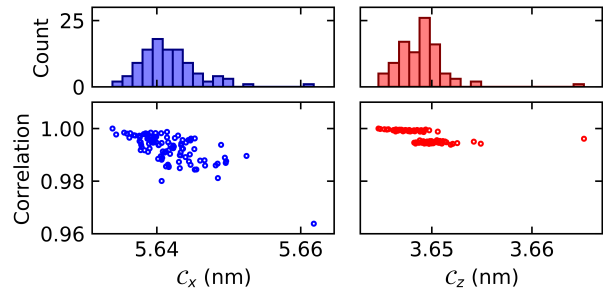


FIG. S3. Field correlation coefficient as a function of the optimized value of the CRLB for x_0 (left panel) and z_0 (right panel). The histograms show the distribution of the optimal value found by the optimization algorithm for 100 different initial guesses. For clarity, three outliers are not shown in the distribution of C_z . The CRLB for these outliers is 3.678 nm, 3.709 nm and 3.738 nm.

In order to determine to what extent the optical modes that are excited are the same for the different solutions, we take the best solution of each coordinate as a reference and we calculate the amplitude of the correlation coefficient for the optimized fields at $z = L_z$ (Fig. S3, bottom panels). The fields associated with the lowest CRLB are highly correlated with the reference field, with a correlation coefficient close to unity. Note that the step-like behavior of the correlation coefficient reflects the possibility for the algorithm to get trapped into a few local optima. Nevertheless, we can see that all the solutions are strongly correlated with the reference field, with a correlation coefficient of at least 0.96. This indicates that, regardless of the initial guess, the optimization algorithm converges towards similar fields distributions.

VI. INTENSITY ENHANCEMENT AT THE TARGET POSITION

We showed in the manuscript that the CRLB scales with $\rho^{-1/2}$ when C_{xz} is minimized. This is a consequence of the linear relation between the excitation intensity at the target position and the LDOS. Indeed, the intensity enhancement resulting from the minimization of C_{xz} scales with the LDOS (Fig. S4), with a correlation coefficient of 0.72 calculated on log-transformed variables. Furthermore, configurations with a high Cramér-Rao bound are characterized by both a small intensity and a low LDOS. Reversely, configurations with a low CRLB are characterized by both a large intensity and a high LDOS. This confirms that the reduction of the CRLB observed for high LDOS is a consequence of the enhancement of the excitation intensity at the target position.

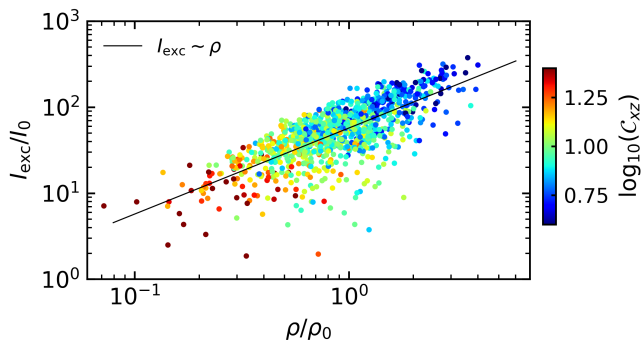


FIG. S4. Enhancement of the excitation intensity at the position of the target as a function of the normalized LDOS for $kl = 9.7$ when C_{xz} is minimized. The color of each point represents the value of C_{xz} , and the black line is a fit to the optimized data by a power law with an exponent equal to 1.

The observed relation between LDOS and intensity enhancement is in agreement with known results obtained in the context of time-reversal experiments. Such experiments, which provide a method to focus waves into complex scattering media [5], can be decomposed as two-step

processes. During a recording step, a dipole source with constant dipole moment d_s is located inside a scattering system, and this source emits a field that is recorded on a given surface by a far-field wavefront sensor. During a time-reversal step, a wavefront generator generates on the same surface an incoming field that is the time-reversed replica of the outgoing field previously recorded. It is then known that the power emitted by the source is proportional to the LDOS [6, 7], and that the intensity of the time-reversed field at the source position is proportional to the product of $|d_s|^2$ and ρ^2 [8]. In order to relate this latter result to our analysis, which is performed for a constant number of photons injected in the scattering system, we must re-normalized the dipole moment of the source d_s by the square root of the LDOS, such that the source emits a constant power regardless of its position. In that case, the resulting intensity at the target position scales with the LDOS, in agreement with our numerical results.

The linear relation between ρ and I_{exc} is strictly valid whenever one has a full control over the input and output modes of the field, which is a necessary condition to achieve a complete time reversal of the field [8]. This is not the case in our numerical simulations, which suggests that the correlation between ρ and I_{exc} could be further improved by performing a more complete control of input and output modes in our simulations.

-
- [1] M. Lax, Phys. Rev. **85**, 621 (1952).
 - [2] S. Kay, *Fundamentals of Statistical Processing, Volume I: Estimation Theory* (Prentice Hall, 1993).
 - [3] J. Alexander Liddle and G. M. Gallatin, *Nanoscale* **3**, 2679 (2011).
 - [4] S. Kirkpatrick, C. D. Gelatt, and M. P. Vecchi, *Science* **220**, 671 (1983).
 - [5] A. P. Mosk, A. Lagendijk, G. Lerosey, and M. Fink, *Nat. Photonics* **6**, 283 (2012).
 - [6] W. L. Barnes, *J. Mod. Opt.* **45**, 661 (1998).
 - [7] R. Carminati, A. Cazé, D. Cao, F. Peragut, V. Krachmalnicoff, R. Pierrat, and Y. De Wilde, *Surf. Sci. Rep.* **70**, 1 (2015).
 - [8] R. Carminati, R. Pierrat, J. de Rosny, and M. Fink, *Opt. Lett.* **32**, 3107 (2007).